ES Energy & Environment

RESEARCH PAPER

View Article Online

Influence of Anti-reflecting Nature of MgF_2 Embedded Electrospun TiO_2 Nanofibers Based Photoanode to Improve the Photoconversion Efficiency of DSSC

Pratheep Panneerselvam,[1] Vignesh Murugadoss,[1,2] Vijayakumar Elayappan,[1,3] Na Lu,[4*] Zhanhu Guo,[2*] and Subramania Angaiah[1*]

TiO_2 nanofibers (NFs) embedded with different weight percentages of magnesium fluoride (MgF_2) are fabricated by electrospinning technique to use as an anti-reflecting photoanode to enhance the power conversion efficiency (PCE) of DSSC. The thermal behaviour of TiO_2/PVP and TiO_2/PVP/MgF_2 precursors are studied by TG/DTA analysis. The MgF_2 embedded electrospun TiO_2 NFs has mixed phases of anatase and rutile and their weight fractions are investigated by X-ray diffraction analysis. The MgF_2 embedded electrospun TiO_2 NFs exhibited high dye loading compared to bare TiO_2 NFs. The surface morphology of MgF_2 embedded electrospun TiO_2 NFs is investigated by FE-SEM and TEM analysis. Among the different wt.% of MgF_2 embedded electrospun TiO_2 NFs, 10 wt% MgF_2 embedded TiO_2 NFs based DSSC enhanced the light harvesting effectively and thereby increase the PCE to 5.56%, which is an increase of 17% compared to bare electrospun TiO_2 NFs based DSSC (4.76%).

Keywords: Dye-sensitized solar cell; TiO_2 nanofibers; Magnesium fluoride; Anti-reflecting photoanode.

Received 19 September 2018**, Accepted** 20 October 2018

DOI: 10.30919/esee8c153

1. Introduction

Dye-sensitized solar cell (DSSC) is a low-cost solar cell and an alternative to conventional solar cell demonstrated by Michael Gratzel in the year 1991. This invention has attracted much because it does not require ultra-high pure materials, unlike silicon solar cell.[1] Many researchers are taking the effort to improve the overall PCE by modifying the photoanode, counter electrode, dye, and electrolyte.[2-5] Among them, the light harvesting nature of solar cell mainly depends on the photoanode.[6,7] The photoanode fabricated from TiO_2 nanoparticles, the electrons transport are limited by the resistance of electrons in traps and the structural disorder at the contact among the nanoparticles leads to a reduction in the collection of the injected electrons.[8] On the contrary, one-dimensional (1D) nanostructures consist of an almost defect-free structure which can provide a direct and quick pathway for the electrons with a limited interfacial recombination[9] and also provide excellent mobility of charge carriers that enhance the charge collection and transport.[10-15] Use of 1D TiO_2 nanomaterial instead of TiO_2 nanoparticles decreases the ohmic loss during the transport of injected electrons.[16,17] The electrospinning technique is a simple, versatile and cost-effective to produce 1D nanostructured materials.[18] There are many strategies to enhance the cell efficiency where one of the effective methods to enhance the light harvesting capability is via improved light transport by introducing anti-reflective material into the photoanode so that the dye has an opportunity to absorb more photons and consequently generate more number of free carriers for DSSC. In the recent scenario, ZnO and SiO_2 are widely used as anti-reflecting materials for DSSC.[17,19] To the best of our knowledge, so far no one has reported that MgF_2 as an anti-reflecting material for DSSC applications. The MgF_2 has a low refractive index value of 1.35 with high positive isoelectric point (IEP) which may increase the light harvesting capability and dye adsorption nature of the system.

In the present investigation, a new anti-reflective nanostructured photoanode is developed by embedding anti-reflecting material (MgF_2) in the randomly aligned TiO_2 nanofibers (NFs) by electrospinning process and its influence on the adsorption of dye, anti-reflecting effect on its PCE are studied in details.

[1]*Electro-Materials Research Laboratory, Centre for Nanoscience and Technology,Pondicherry University, Puducherry-605 014, India.*
[2]*Integrated Composites Laboratory, Department of Chemical and Biomolecular Engineering, University of Tennessee, Knoxville, Tennessee 37996, USA*
[3]*Department of Chemical Engineering, Yeungnam University, Gyeongsan, Gyeongbuk-38541, Republic of Korea*
[4]*School of Materials Engineering, Purdue University, Indiana 47907-2045, USA*
***E-mail:** luna@purdue.edu (N.L); zguo10@utk.edu (Z.G); a.subramania@gmail.com (S.A)*

2. Experimental procedure

2.1 Materials

MgF_2 embedded electrospun TiO_2 NFs were fabricated from titanium (IV) isopropoxide (Sigma-Aldrich), polyvinylpyrrolidone (PVP, Aldrich), acetic acid (Merck) and magnesium fluoride (Himedia). The photoanode paste was prepared from ethyl cellulose (EC, Ottokemi), terpineol (Himedia) and dibutyl phthalate (Merck). A fluorine-doped tin oxide glass plate (FTO, TEC-7 and 2.2 mm) and N719 dye (Sigma-Aldrich) were used.

2.2 Fabrication of pure and MgF_2 embedded TiO_2 NFs

Pure and MgF_2 embedded electrospun TiO_2 NFs were fabricated by electrospinning method with the following procedure; the precursor solutions composed of 2.7 g of titanium (IV) isopropoxide, 2.5 mL of acetic acid, 2.5 mL of ethanol and 15 mL of 5 wt.% polyvinylpyrrolidone (PVP) along with two different wt.% of MgF_2 (5 and 10 wt.%) added with continuous stirring for 12 h to get viscous solutions.[20] They were then loaded separately into a syringe connected with a 27 gauge stainless steel needle. The applied potential and the collector distance from the tip of the needle were fixed as 24 kV and 12 cm, respectively. The flow rate of the solution was 0.5 mL h^{-1} to get the MgF_2 embedded electrospun TiO_2 mats. They were removed from the collector and kept in a vacuum oven at 80 ºC for 6 h. They were then calcined at 500 ºC for 4 h to get both pure and MgF_2 embedded electrospun TiO_2 NFs.

2.3 Characterization of pure and MgF_2 embedded TiO_2 NFs

The physical characterization such as TG/DTA and X-Ray diffraction analysis (XRD) were carried out as per the procedure given in our previous studies.[20-22] The band gap, dye adsorption and anti-reflecting properties of the prepared TiO_2 and MgF_2 embedded TiO_2 NFs were studied by UV-Vis spectrometer.[20,21] The morphology of the prepared TiO_2 and MgF_2 embedded TiO_2 NFs were studied by FE-SEM and TEM analysis. The Raman spectra and Photoluminescence characterization were also done as per the procedure given in our previous studies.[20,21] Electrochemical AC-impedance analysis was made in the frequency range of 1m Hz to 100 kHz with an AC amplitude of 10 mV. For all physical characterization, we used uniform coating thickness of 12 µm for all the studied systems.

2.4 Photovoltaic performance of DSSCs

The photovoltaic performance of DSSCs fabricated by using both pure and MgF_2 embedded TiO_2 NFs as photoanodes were examined by AM 1.5 solar simulator (Newport, Oriel Instruments, USA 150 W; Model: 67005) and a light intensity of 100 mWcm^{-2} with a computer controlled digital source meter (Keithley, Model: 2420) as described elsewhere.[20,21] We fabricated three DSSCs for each system to study their photovoltaic performances.

3. Results and discussion

3.1 Thermal behaviour and structural properties

Fig. 1a shows the thermal behaviour of electrospun pure PVP/TiO_2 and MgF_2/PVP/TiO_2 precursors. According to the TG curve, ~25% of weight loss has identified for PVP/TiO_2 and MgF_2/PVP/TiO_2 samples in the temperature range of 35 °C to 200 °C. The major weight loss of ~44% and ~35% have identified in the region of 350 °C to 550 °C for PVP/TiO_2 and MgF_2/PVP/TiO_2 samples, respectively. These results indicate that while embedding MgF_2 in TiO_2 NFs, the weight loss reduced and there is no decomposition of MgF_2 in that region. The evaporation of solvent molecules and other organic residues are indicated by a long endothermic peak at ~90 °C for MgF_2/PVP/TiO_2 sample and ~100 °C for PVP/TiO_2 sample. A small exothermic peak in the range of ~340 °C to 400 °C is observed for both the samples is due to the decomposition of PVP on the main chain.[23] A weak endothermic peak at ~450 °C indicates the phase change of TiO_2 from amorphous to anatase is found in the DTA curve. At the same time, there is no weight loss after 470 °C in the TG curve.

Fig. 1b shows the XRD pattern of pure TiO_2 NFs and MgF_2 embedded TiO_2 NFs calcined at 500 °C. For pure TiO_2 NFs, the XRD pattern well index to the anatase phase and non-appearance of diffraction peaks at 27° and 31° (Fig. S1) specify that the TiO_2 sample is free from the rutile and brookite structure. The MgF_2 embedded TiO_2 NFs exhibit mixed phases of anatase and rutile. From the XRD result, the weight fraction of these two phases calculated from the following equation:[24]

$$W_R = \frac{I_R}{(0.884\times I_A)+I_R} \tag{1}$$

where W_R, I_A, and I_R represent rutile weight percentage, the integrated intensity of anatase (101) and rutile (110) peaks, respectively. The calculated rutile content by the addition of 5 and 10 wt.% MgF_2 in TiO_2 NFs are approximately 26% and 17%, respectively. The rutile content is reduced by addition of 10 wt.% MgF_2 in TiO_2 NFs because MgF_2 is a rutile compound, and hence while adding, it induces the rutile nature of TiO_2. Beside that, the interaction of Mg^{2+} with Ti^{4+} also induces the rutile nature. But, while adding 10 wt.% MgF_2, Mg^{2+} may form MgO during calcination process and hence the rutile nature is reduced to17% when compared to the addition of 5 wt.% MgF_2 in TiO_2 NFs.[25-27]

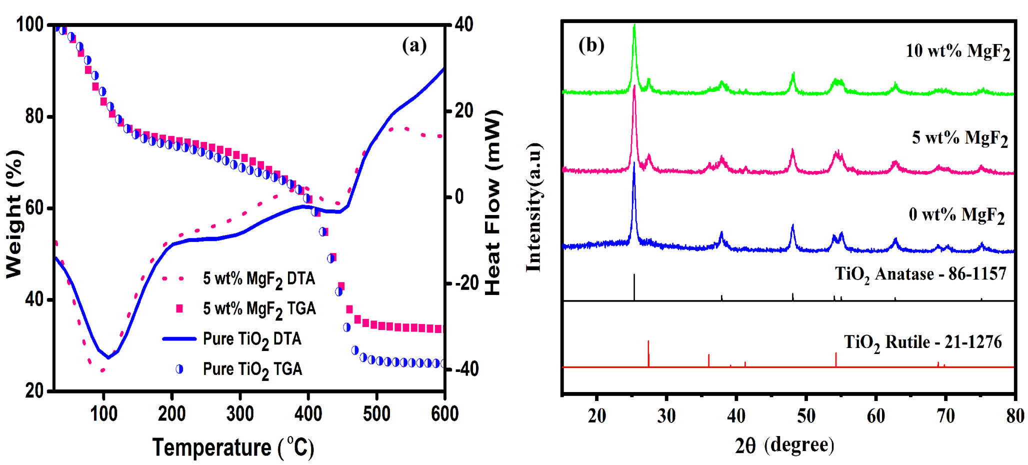

Fig. 1 (a) Thermal analysis of pure TiO_2 and MgF_2 embedded TiO_2 precursor samples; (b) XRD patterns of pure and MgF_2 embedded TiO_2 NFs calcined at 500 °C.

Fig. 2 shows the Raman spectra of pure and MgF_2 embedded TiO_2 NFs. There is no secondary peak related to rutile, MgF_2 Mg and its oxide. The normal modes of vibration for pure TiO_2 tetragonal anatase phase are identified at 142 (E_g), 196 (E_g), 396 (B_{1g}), 515 (A_{1g} + B_{1g}) and 638 cm^{-1} (E_g). For 5 wt.% MgF_2 embedded TiO_2 NFs, the normal modes of vibration are observed at 145 (E_g), 196 (E_g), 393 (B_{1g}), 522(A_{1g} + B_{1g}) and 640 cm^{-1} (E_g). Raman peaks are observed at 144 (E_g), 196 (E_g), 396 (B_{1g}), 515 (A_{1g} + B_{1g}) and 638 cm^{-1} (E_g) for 10 wt.% MgF_2 embedded TiO_2 NFs. These results are matched with previously reported values.[27] The E_g peak corresponds to O−Ti−O symmetric stretching vibration of TiO_2, B_{1g} peak corresponds to symmetric bending vibration of O−Ti−O, and the A_{1g} peak corresponds to O−Ti−O anti-symmetric bending vibration of TiO_2.[28] Changes in the Raman shift is mainly at low-frequency E_g peak and high-frequency E_g peak. The intensity of Raman lines at low-frequency E_g peak value drastically decrease for 5 wt.% MgF_2 embedded TiO_2 NFs compared to the pure and 10 wt.% MgF_2 embedded TiO_2 NFs and the intensity of Raman line increases for 10 wt.% MgF_2 embedded TiO_2 NFs when compared to pure and 5 wt.% MgF_2 embedded TiO_2 NFs. The reason for changes in the E_g peak is due to the disorder induced and phonon confinement effect by the embedded MgF_2, which affects the lattice vibrational characteristics and also induces the change in the Raman lines of TiO_2 NFs.[29]

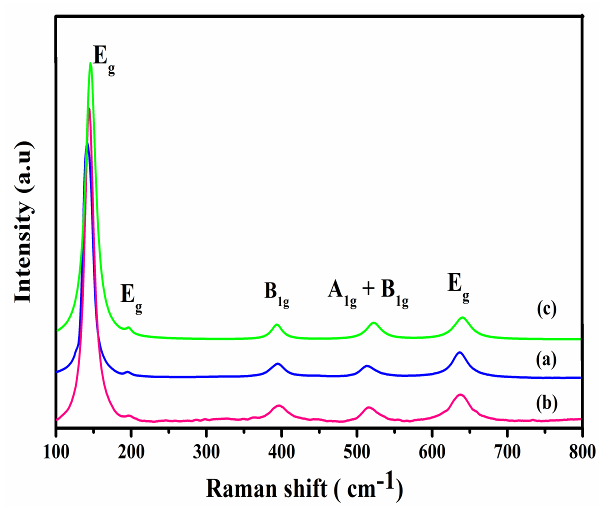

Fig. 2 Raman spectra of (a) pure TiO_2 NFs; (b) 5 wt.% MgF_2 embedded TiO_2 Nfs; (c) 10 wt.% MgF_2 embedded TiO_2 NFs.

3.2 Optical and morphology properties

Fig. 3a shows the absorption of pure TiO_2 NFs and MgF_2 embedded TiO_2 NFs. The maximum absorption in the range of 380 nm to 200 nm is due to the addition of MgF_2 in TiO_2. The band gaps of the prepared sample have changed from 3.20 eV to 3.19 eV by the addition of MgF_2 in TiO_2 NFs (Fig. S2). The bandgap of 5 wt. % of MgF_2 embedded TiO_2 NFs has 3.13 eV, where the rutile phase is 26%. But the band gap of pure TiO_2 rutile phase is 3.0 eV and its pure anatase phase is 3.2 eV.[30] The decrease in band gap is due to the high rutile phase concentration. The 10 wt.% of MgF_2 embedded TiO_2 NFs has a bandgap of 3.19 eV where the rutile phase is 17%, due to the decrease of rutile phase of the system, which increased the band gap to 3.19 eV. The relationship between the flat-band potential, V_{fb} (NHE) and the band gap, E_g is given by Eq. (2).[31] Accordingly, the flat-band potential of 10 wt.% MgF_2 embedded TiO_2 NFs (-0.25 eV) sample lies at the position slightly lesser than pure TiO_2 (-0.26 eV) and for 5 wt.% MgF_2 embedded TiO_2 NFs (-0.19 eV) sample, the V_{fb} is also lying at more positive side than other two samples. Due to more shift in the V_{fb} affects the electron transfer to the FTO glass for DSSC fabricated by using 5 wt.% MgF_2 embedded TiO_2 NFs as photoanode.

$$V_{fb}(NHE) = 2.94 - E_g \quad (2)$$

Fig. 3b shows the transmittance spectra of pure TiO_2 NFs and MgF_2 embedded TiO_2 NFs. The pure TiO_2 NFs sample has exhibited less transmittance of light in the region of 400-550 nm, whereas MgF_2 embedded TiO_2 NFs exhibited an increase in transmittance of light. This is due to the low refractive index of MgF_2 (1.35), which produce high anti-reflecting nature. The increment in the transmittance is greatly dependent on their refractive index.[32-34] This result indicates that 10 wt.% MgF_2 embedded TiO_2 NFs works as a good anti-reflective material and the incident light loss has much lesser than other two photoanodes fabricated by using pure TiO_2 NFs and 5 wt.% of MgF_2 embedded TiO_2 NFs. The absorption peak of N719 dye on the photoanode fabricated by using pure TiO_2 NFs and MgF_2 embedded TiO_2 NFs are observed at 500-550 nm, where the higher dye absorption has observed in 5 wt.% and 10 wt.% of MgF_2 embedded TiO_2 NFs (Fig. 3c). This can be explained by using the isoelectric point (IEP) of MgF_2 and TiO_2 which have IEPs of 9.5 and 6.2, respectively.[8,35] While immersing the photoanodes in the dye solution, the oxide surface gets a positive charge and dye molecules

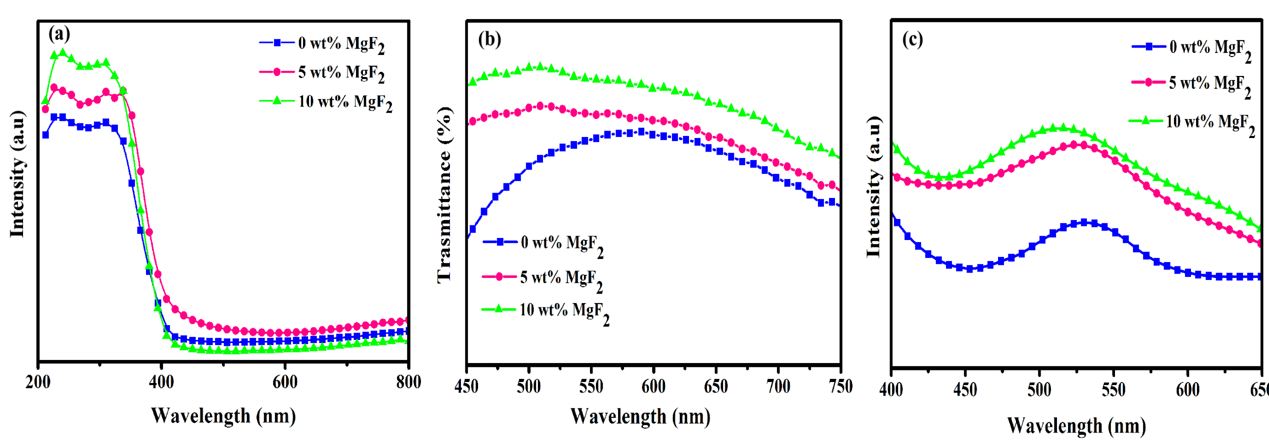

Fig. 3 (a) UV-Vis absorption spectra; (b) Transmittance spectra of pure TiO_2 NFs and MgF_2 embedded TiO_2 NFs; (c) Absorption spectra of N719 dye adsorbed on pure TiO_2 NFs and MgF_2 embedded TiO_2 NFs photoanodes.

get a negative charge. MgF_2 more positive than TiO_2 and hence the MgF_2 embedded TiO_2 NFs has higher dye loading than the pure TiO_2 NFs.[8] The transmittance spectrum of the low refractive index of MgF_2 has higher transmittance and this is one of the key points to explain the higher dye loading on the system, which has a lower refractive index compared to the pure TiO_2 NFs. The refractive index is also related to porosity and hence the introduction of porosity also yields the low refractive index on the system.[32,33,36,37] These results revealed the enhanced dye loading and photovoltaic performance of MgF_2 embedded TiO_2 NFs.

Fig. 4a&b shows FE-SEM images of electrospun pure TiO_2 and MgF_2 embedded TiO_2 mat before calcination. The electrospun TiO_2 NFs appear quite smooth due to its amorphous nature. Each individual TiO_2 NFs are quite uniform in cross-section with an average diameter of 200 nm. Fig. 4c&d show the FE-SEM image of pure TiO_2 NFs and MgF_2 embedded TiO_2 NFs after calcination. Its diameter is appeared to decrease from 200 to 90 nm. Energy dispersive spectra (EDS) of pure TiO_2 NFs and 10 wt.% of MgF_2 (Fig. S3) embedded TiO_2 NFs confirmed that the MgF_2 present in the TiO_2 NFs.

Fig. 5a&b shows the typical TEM images of 10 wt.% MgF_2 embedded TiO_2 NFs and its average diameter is found to be ~100 nm and whereas the individual TiO_2 NF is made up of arrays of nanocrystals. The HRTEM image (Fig. 5c) shows the plane orientation of different phases present in 10 wt.% MgF_2 embedded TiO_2 NFs. Fig. 5c indicates that the interplanar spacing of 0.35 nm, 0.25 nm and 0.32 nm corresponding to TiO_2 anatase, TiO_2 rutile, and MgF_2 phases, respectively. Fig. 5d shows the selected area electron diffraction (SAED) pattern which confirms that the MgF_2 embedded TiO_2 NFs is composed of polycrystalline phase. The Debye-Scherrer concentric rings correspond to the phases denoted as A, R, and M which correspond to anatase, rutile and magnesium fluoride, respectively and their planes are indexed in SAED pattern (Fig. 5d).

Fig. 6 shows PL emission spectra of pure TiO_2 NFs, 5 and 10 wt.% MgF_2 embedded TiO_2 NFs excited at 290 nm. All the three samples showed a similar PL pattern with a strong emission band at 378 nm. The photocurrent generation process in DSSC generally includes charge separation, charge transport, and charge recombination. It is well reported that the external embedded carriers will control the electron-hole separation at the host semiconductor electrode. Among the three samples, 10 wt.% MgF_2 embedded TiO_2 NFs have exhibited much lower emission intensity than pure TiO_2 NFs and 5 wt.% MgF_2 embedded TiO_2 NFs. It indicates that the recombination of photoinduced charge carrier was greatly inhibited in 10 wt.% MgF_2 embedded TiO_2 NFs based heterojunction system,[38,39] which implies high PCE of the system.

3.3 Electrochemical and photovoltaic performance of DSSCs

The electrochemical impedance studies explain the internal resistance of DSSC. The impedance spectra of DSSCs fabricated using pure TiO_2 NFs and MgF_2 embedded TiO_2 NFs as photoanodes are shown in Fig. 7a. The Nyquist plot exhibits two semicircles, the small semicircle at higher frequency corresponds to the charge transfer resistance at the interface of the redox electrolyte/Pt counter electrode (R_{ct1}) and the larger semicircle at lower frequency corresponds to charge transfer resistance at TiO_2 NFs/dye/electrolyte interface (R_{ct2}). The Warburg diffusion process of I^-/I_3^- redox couple in an electrolyte (Z_w) is virtually overlapped by R_{ct2}. The larger

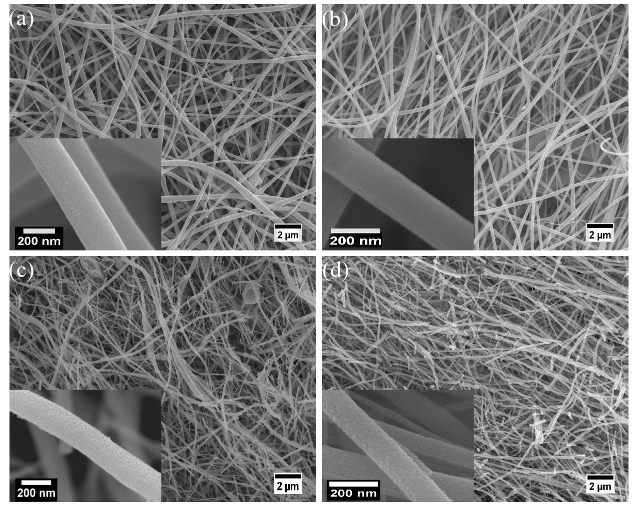

Figure 4. FE-SEM image of (a) pure TiO_2 mat; (b) 10 wt.% MgF_2 embedded TiO_2 mat before calcination; (c) pure TiO_2 NFs and (d) 10 wt.% MgF_2 embedded TiO_2 NFs after calcination at 500°C.

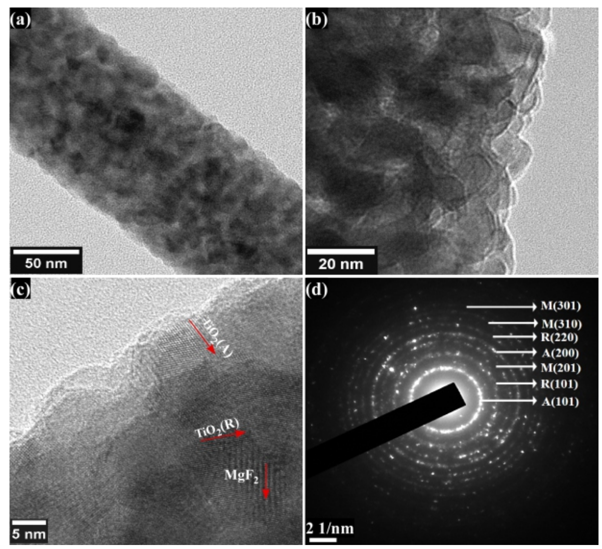

Fig. 5 (a & b) TEM images of 10 wt.% of MgF_2 embedded TiO_2 NFs; (c & d) HRTEM image and SAED pattern of 10 wt.% of MgF_2 embedded TiO_2 NFs.

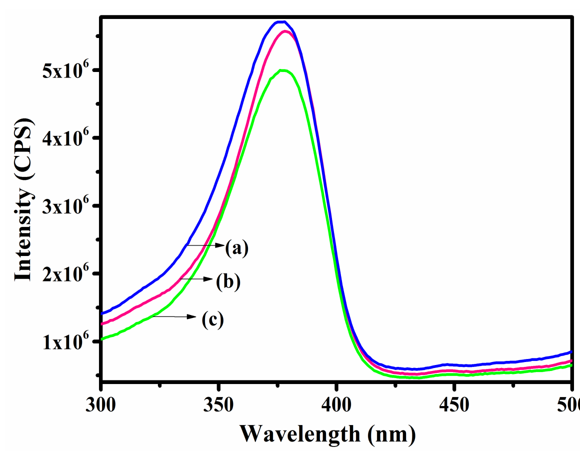

Fig. 6 Photoluminescence emission spectra of (a) pure TiO_2 NFs; (b) 5 wt.% MgF_2 embedded TiO_2 NFs; (c) 10 wt.% MgF_2 embedded TiO_2 NFs.

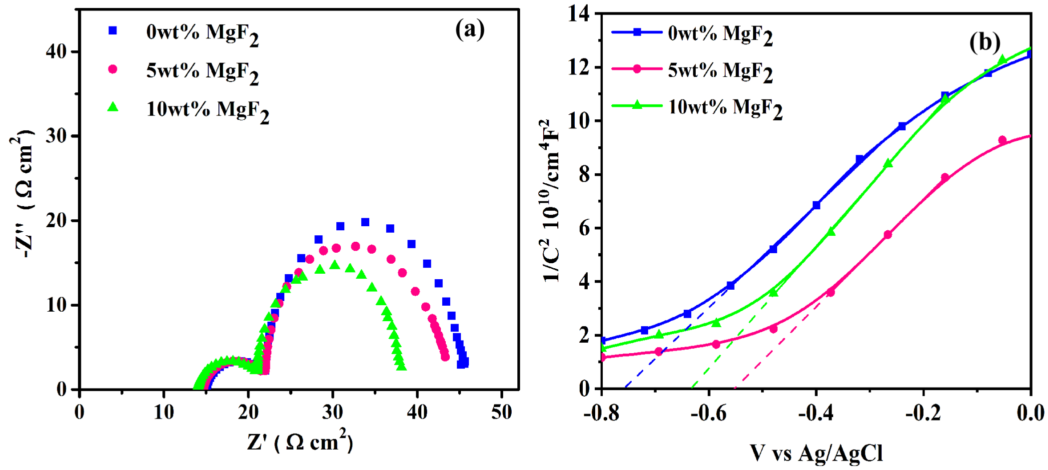

Fig. 7 (a) Impedance spectra; (b) Mott – Schottky electrochemical analysis of pure TiO_2 NFs and MgF_2 embedded TiO_2 NFs**.**

Table 1 Electrochemical impedance parameter values of DSSCs fabricated using pure TiO_2 NFs and MgF_2 embedded TiO_2 NFs as photoanodes.

Photoanode	R_s	R_{ct1} (Ωcm^{-2})	R_{ct2} (Ωcm^{-2})
Pure TiO_2 NFs	15.06	6.89	23.84
5 wt.% MgF_2 embedded TiO_2 NFs	14.90	7.28	22.35
10 wt.% MgF_2 embedded TiO_2 NFs	13.81	6.42	18.09

semicircle decreased with increasing amount of MgF_2. DSSC fabricated by using 10 wt.% MgF_2 embedded TiO_2 NFs as the photoanode has exhibited less R_{ct2} (Table 1) than other two systems.[40]

The MgF_2 embedded system influence the TiO_2 band structure and energy levels which is evaluated with Mott – Schottky (MS) analysis. The MS plots are obtained for pure TiO_2 NFs and MgF_2 embedded TiO_2 NFs photoanodes are shown in Fig. 7b. The plot $1/C^2$ vs Applied Potential (V) exhibits a typical positive slope characteristic of n-type semiconducting behaviour. The flat band potential possibilities are gained by MS plot as acquired by a linear extrapolation to C=0, i.e., the capture at the X-axis.[41] The flat band potential of three samples are -0.63, -0.75, -0.55 V (vs Ag/AgCl). It is noteworthy that the embedded system changes the Fermi level and flat band potential of TiO_2 NFs this is a further witness from UV-Vis analysis.

Fig. 8 represents the photocurrent density-voltage (J-V) curves for DSSCs fabricated by using pure TiO_2 NFs and MgF_2 embedded TiO_2 NFs as photoanodes at a light intensity of 100 mW cm^{-2} under the standard global AM 1.5 irradiation and their corresponding photovoltaic parameters are summarized in Table 2. It shows that the DSSC fabricated by using 10 wt.% MgF_2 embedded TiO_2 NFs as the photoanode has the maximum efficiency of 5.56 % with a short-circuit photocurrent density (J_{sc}) of 11.2 mA/cm^2. MgF_2 is an anti-reflective material which helps to reduce the incident photon loss by reducing the reflection of light and increasing light absorption of dye molecules in the system. This leads to more electron generation which results in high photocurrent density.

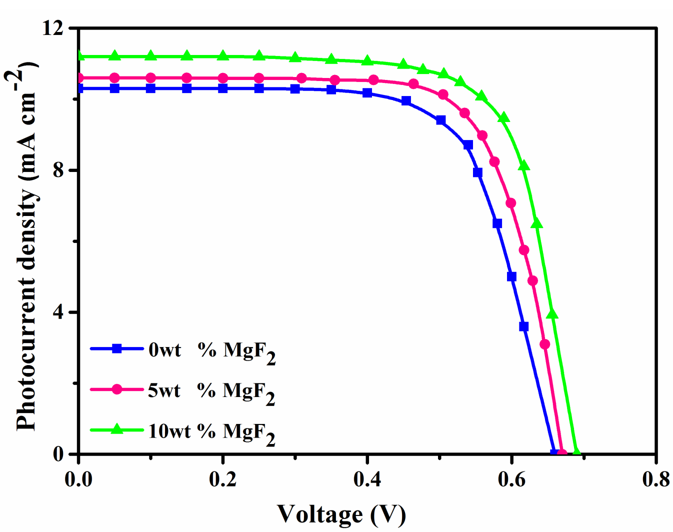

Fig. 8 J-V curves of DSSCs fabricated with different wt.% of MgF_2 embedded TiO_2 NFs as photoanodes.

Table 2 Photovoltaic parameter values of DSSCs fabricated with different weight pecent of MgF_2 embedded TiO_2 NFs as photoanodes.

MgF_2 wt.%	J_{sc} ($mA\,cm^{-2}$)	V_{oc} (V)	FF	η (%)
0	10.3	0.66	0.70	4.76
5	10.6	0.67	0.71	4.95
10	11.2	0.69	0.72	5.56

The photocurrent density (J_{sc}) is directly proportional to the physical parameter of the cell which is given by the Eq. (3):[42]

$$J_{sc} = I_0 \, \Phi_{LH} \, \Phi_{CS} \, \Phi_{COL} \quad (3)$$

where I_0 is the incident photon flux, Φ_{LH} is the fraction of incident light absorbed by the dye is termed as light harvesting efficiency and is determined by the amount of dye present in the system, Φ_{CS} is the quantum efficiency of charge separation in the event. Φ_{COL} is the fraction of the separated charges measured as photocurrent under short circuit condition is termed as collection efficiency. The DSSC fabricated by using 10 wt.% MgF_2 embedded TiO_2 NFs as the photoanode exhibited higher photocurrent density compared to pure TiO_2 NFs and 5 wt.% MgF_2 embedded TiO_2 NFs based DSSC systems due to the higher light absorption of dye (Φ_{LH}) and the mixed phase of anatase and an optimum amount of rutile structure was good for electron transport. According to the PL study, the highest charge separation efficiency (Φ_{CS}) of photoinduced electron-hole pairs occurred in the heterojunction system. According to the equation (3), the higher charge separation efficiency (Φ_{CS}) and higher light absorption of dye (Φ_{LH}) imply the higher photocurrent density and higher power conversion efficiency than the pure TiO_2 NFs and 5 wt.% MgF_2 embedded TiO_2 NFs based DSSCs. But the DSSC fabricated by using 5 wt.% MgF_2 embedded TiO_2 NFs as the photoanode has higher light absorption of dye which leads to producing more electrons but due to the reduction in band gap the conduction band level has much reduced so the electrons diffused through the TiO_2 NFs is much reduced which reduced the charge separation efficiency (Φ_{CS}) that reduced the PCE.

4. Conclusion

Both, pure TiO_2 NFs and MgF_2 embedded TiO_2 NFs were successfully fabricated by electrospinning process. The thermal studies showed complete crystallization temperature of the prepared precursor sample and it was found to be 500 °C. The evolution of rutile phase was analyzed by XRD and the weight fraction of the anatase and rutile phases were calculated from the anatase (101) and rutile (110) peaks. The shift in flat band potential, optical band gap and the dye adsorption nature of the photoanodes were analyzed by UV-Vis spectroscopy. The surface morphology was revealed by FE-SEM and TEM images of the prepared TiO_2 NFs and MgF_2 embedded TiO_2 NFs. The photovoltaic performance of DSSC fabricated by using 10 wt.% MgF_2 embedded TiO_2 NFs as photoanode exhibited the maximum light to electricity efficiency (η) of 5.56% with 17% improvement than that fabricated with pure TiO_2 NFs as photoanode.

Conflicts of interest

The authors declare that they have no conflict of interest.

Acknowledgements

The authors gratefully acknowledge the CIF of Pondicherry University for extending the instrumentation facilities. Dr. AS gratefully acknowledges the CSIR, New Delhi for providing the financial support (No.01(2810)/14/EMR-II). Mr. MV is grateful to the Indo-US Science and Technology Forum (IUSSTF), Department of Science and Technology (DST), New Delhi for providing a fellowship under the BASE program (IUSSTF BASE Internships 2018/ 12/ Vignesh M, dt. 09/04/2018).

References

1. A. Jena, S. P. Mohanty, P. Kumar, J. Naduvath, V. Gondane, P. Lekha, J. Das, H. K. Narula, S. Mallick and P. Bhargava, *Trans. Indian Ceram. Soc.*, 2012, **71**, 1-16.
2. Subramania A, Vighnesh M, Subasri A and Sarathkumar K, *Eng. Sci.*, 2018, In press, www.doi.org/10.30919/es8d756.
3. V. Murugadoss, N. Wang, S. Tadakamalla, B. Wang, Z. Guo and S. Angaiah, *J. Mater. Chem. A*, 2017, **5**, 14583-14594.
4. V. Elayappan, V. Murugadoss, S. Angaiah, Z. Fei and P. Dyson, *J. Appl. Polym. Sci.*, 2015, **132**, 42777.
5. Z. Salam, E. Vijayakumar, A. Subramania, N. Sivasankar and S. Mallick, *Sol. Energy Mater. Sol. Cells*, 2015, **143**, 250-259.
6. T. Liu, J. Hou, B. Wang, F. Bai, H. Chen, L. Gao, Y. Cao, H. He, J. Wang, N. Wang, G. Cao and Z. Guo, *J. Mater. Chem. A*, 2016, **4**, 10794-10800.
7. S. K. Kim, M. K. Son, S. Park, M. S. Jeong, H. Seo, K. Prabakar and H. J. Kim, *Electron. Mater. Lett.*, 2014, **10**, 229-234.
8. H. Park, D. J. Yang, H. G. Kim, S. J. Cho, S. C. Yang, H. Lee and W. Y. Choi, *J. Electroceram.*, 2009, **23**, 146-149.
9. E. H. Kong, Y. H. Yoon, Y. J. Chang and H. M. Jang, *Mater. Chem. Phys.*, 2014, **143**, 1440-1445.
10. L. Yang, X. Wang, X. Mai, T. Wang, C. Wang, X. Li, V. Murugadoss, Q. Shao, S. Angaiah and Z. Guo, *J. Colloid Interface Sci.*, 2018, In press, https://doi.org/10.1016/j.jcis.2018.09.045.
11. X. Feng, K. Shankar, O. K. Varghese, M. Paulose, T. J. Latempa and C. A. Grimes, *Nano Lett.*, 2008, **8**, 3781-3786.
12. Z. R. Tian, J. A. Voigt, J. Liu, B. McKenzie and H. Xu, *J. Am. Chem. Soc.*, 2003, **125**, 12384-12385.
13. K. Zhu, N. R. Neale, A. Miedaner and A. J. Frank, *Nano Lett.*,

2007, **7**, 69-74.
14. G. K. Mor, K. Shankar, M. Paulose, O. K. Varghese and C. A. Grimes, *Nano Lett.*, 2006, **6**, 215-218.
15. P. Zhu, A. S. Nair, P. Shengjie, Y. Shengyuan and S. Ramakrishna, *ACS Appl. Mater. Interfaces*, 2012, **4**, 581-585.
16. J. Jiu, S. Isoda, F. Wang and M. Adachi, *J. Phys. Chem. B*, 2006, **110**, 2087-2092.
17. H. Li, B. Jiang, R. Schaller, J. Wu and J. Jiao, *J. Phys. Chem. C*, 2010, **114**, 11375-11380.
18. G. Zhu, L. Pan, J. Yang, X. Liu, H. Sun and Z. Sun, *J. Mater. Chem.*, 2012, **22**, 24326-24329.
19. Y. Wang, E. Chen, H. Lai, B. Lu, Z. Hu, X. Qin, W. Shi and G. Du, *Ceram. Int.*, 2013, **39**, 5407-5413.
20. V. Elayappan, P. Panneerselvam, S. Nemala, K. S. Nallathambi and S. Angaiah, *Appl. Phys. A*, 2015, **120**, 1211-1218.
21. P. Pratheep, E. Vijayakumar and A. Subramania, *Appl. Phys. A*, 2015, **119**, 497-502.
22. A. S. Nair, Z. Peining, V. J. Babu, Y. Shengyuan and S. Ramakrishna, *Phys. Chem. Chem. Phys.*, 2011, **13**, 21248-21261.
23. Y. K. Du, P. Yang, Z. G. Mou, N. P. Hua and L. Jiang, *J. Appl. Polym. Sci.*, 2005, **99**, 23-26.
24. J. Ding, Y. Li, H. Hu, L. Bai, S. Zhang and N. Yuan, *Nanoscale Res. Lett.*, 2013, **8**, 9.
25. D. S. Hwang, N. H. Lee, D. Y. Lee, J. S. Song, S. H. Shin and S. J. Kim, *Smart Mater. Struct.*, 2006, **15**, S74.
26. K. K. Kim and A. S. Nowick, *J. Phys. C: Solid State Phys.*, 1977, **10**, 509.
27. D. S. Hwang, Y. I. Cho, N. H. Lee, H. G. Lee, D.-H. Cho and S. J. Kim, *Key Eng. Mater.*, 2004, **264-268**, 21-24.
28. F. Tian, Y. Zhang, J. Zhang and C. Pan, *J. Phys. Chem. C*, 2012, **116**, 7515-7519.
29. W. F. Zhang, Y. L. He, M. S. Zhang, Z. Yin and Q. Chen, *J. Phys. D: Appl. Phys.*, 2000, **33**, 912.
30. B. Choudhury, S. Bayan, A. Choudhury and P. Chakraborty, *J. Colloid Interface Sci.*, 2016, **465**, 1-10.
31. S. Iwamoto, Y. Sazanami, M. Inoue, T. Inoue, T. Hoshi, K. Shigaki, M. Kaneko and A. Maenosono, *ChemSusChem*, 2008, **1**, 401-403.
32. F. Chi, L. Yan, H. Lv, H. Yan, X. Yuan and B. Jiang, *Nanosci. Nanotechnol. Lett.*, 2012, **4**, 441-444.
33. S. Chhajed, M. F. Schubert, J. K. Kim and E. F. Schubert, *Appl. Phys. Lett.*, 2008, **93**, 251108.
34. L. Zhang, Y. Li, J. Sun and J. Shen, *Langmuir*, 2008, **24**, 10851-10857.
35. I. Sevonkaev and E. Matijević, *Langmuir*, 2009, **25**, 10534-10539.
36. Y. Du, L. E. Luna, W. S. Tan, M. F. Rubner and R. E. Cohen, *ACS Nano*, 2010, **4**, 4308-4316.
37. M. S. Park, Y. Lee and J. K. Kim, *Chem. Mater.*, 2005, **17**, 3944-3950.
38. J. Choi, P. Sudhagar, P. Lakshmipathiraj, J. W. Lee, A. Devadoss, S. Lee, T. Song, S. Hong, S. Eito, C. Terashima, T. H. Han, J. K. Kang, A. Fujishima, Y. S. Kang and U. Paik, *RSC Adv.*, 2014, **4**, 11750-11757.
39. Z. Zhang, C. Shao, X. Li, Y. Sun, M. Zhang, J. Mu, P. Zhang, Z. Guo and Y. Liu, *Nanoscale*, 2013, **5**, 606-618.
40. A. M. Cant, F. Huang, X. L. Zhang, Y. Chen, Y.-B. Cheng and R. Amal, *Nanoscale*, 2014, **6**, 3875-3880.
41. X. Jin, Q. Li, Y. Li, Z. Chen, T.-H. Wei, X. He and W. Sun, *Sci. Rep.*, 2014, **4**, 5983.
42. B. C. O'Regan, J. R. Durrant, P. M. Sommeling and N. J. Bakker, *J. Phys. Chem. C*, 2007, **111**, 14001-14010.